Check for updates

Sub-kHz linewidth, hybrid III-V/silicon wavelength-tunable laser diode operating at the application-rich 1647-1690 nm

JIA XU BRIAN SIA,[1,2] ⬤ XIANG LI,[3] WANJUN WANG,[1,5] ZHONGLIANG QIAO,[1] XIN GUO,[1] JIN ZHOU,[1] CALLUM G. LITTLEJOHNS,[4] CHONGYANG LIU,[3] GRAHAM T. REED,[1,4] AND HONG WANG[1,2,6]

[1]*School of Electrical and Electronic Engineering, Nanyang Technological University, 50 Nanyang Avenue, 639798, Singapore*
[2]*Nanyang Nanofabrication Centre, Nanyang Technological University, 50 Nanyang Avenue, 639798, Singapore*
[3]*Temasek Laboratories, Nanyang Technological University, 50 Nanyang Avenue, 637553, Singapore*
[4]*Optoelectronics Research Centre, University of Southampton, Southampton SO17 1BJ, UK*
[5]*wang.wanjun@ntu.edu.sg*
[6]*ewanghong@ntu.edu.sg*

Abstract: The wavelength region about of 1650 nm enables pervasive applications. Some instances include methane spectroscopy, free-space/fiber communications, LIDAR, gas sensing (i.e. C_2H_2, C_2H_4, C_3H_8), surgery and medical diagnostics. In this work, through the hybrid integration between an III-V optical amplifier and an extended, low-loss wavelength tunable silicon Vernier cavity, we report for the first time, a III-V/silicon hybrid wavelength-tunable laser covering the application-rich wavelength region of 1647-1690 nm. Room-temperature continuous wave operation is achieved with an output power of up to 31.1 mW, corresponding to a maximum side-mode suppression ratio of 46.01 dB. The laser is ultra-coherent, with an estimated linewidth of 0.7 kHz, characterized by integrating a 35 km-long recirculating fiber loop into the delayed self-heterodyne interferometer setup. The laser linewidth is amongst the lowest in hybrid/heterogeneous III-V/silicon lasers.

1. Introduction

The development of highly-coherent laser sources through the hybrid/heterogeneous integration of III-V gain media and extended passive silicon photonic low-loss laser cavities has disparaged the notion that the poor light emission properties of silicon would hinder the viability of CMOS-compatible silicon photonics as a photonic platform. As a matter of fact, the extent of coherence with regards to the abovementioned lasers are largely attributed to the lack of spontaneous emission events amongst passive silicon waveguides. By increasing the ratio of optical mode volume between low-loss silicon photonics and III-V gain section via passive laser cavity extension, impressive ultra-narrow linewidths that would be challenging in a solitary laser has been reported [1–5]. Figure 1 illustrates an overview of III-V/silicon hybrid/heterogeneous lasers reported across different wavelength regions and the associated laser linewidths [2–15]. In a III-V/silicon hybrid/heterogeneous integration framework, sub-kHz laser linewidth was only realized recently in 2019 [2,5]. This opens the door for such lasers to be used in applications with a stringent requirement on laser coherence such as compact atomic clocking, GPS systems, highly-precise metrology, driver for Brillouin/Raman lasers, coherent communication/sensing and RF photonics [2–3]. However, III-V/silicon hybrid/heterogeneous lasers reporting sub-kHz linewidths are rare and restricted from the S- to L-band thus far. There is room for the development

of highly-coherent laser sources targeting other application-rich wavelength regions, encouraged by the potential of silicon photonics to operate at longer wavelengths [16], and ability for III-V to be bandgap engineered [17–18].
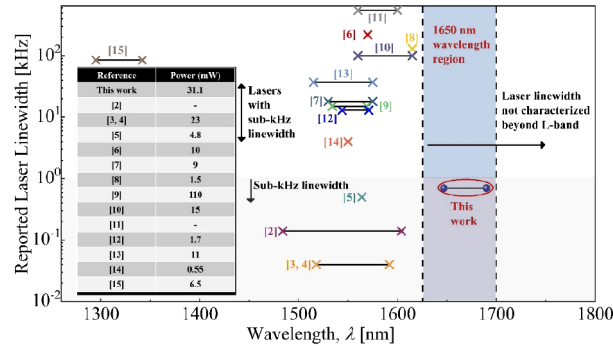
Fig. 1. Overview of III-V/silicon hybrid/heterogeneous laser linewidth reported across different wavelength regions [2–15] in comparison to this work; the corresponding laser output power is tabulated at the inset. Tunable lasers are illustrated by a black line that join two crosses of the same color, indicating the maximum tuning range of the laser.

The wavelength region about 1650 nm can enable widespread applications (Fig. 1). The low propagation loss of the wavelength region in silica fibers [19] and the demonstration of corresponding fiber amplifiers [20–21] addresses the propagation and amplification aspects of telecommunication respectively, potentially increasing the bandwidth of the present communication infrastructure. Natural gas in which methane constitutes 95%, has a propensity to leak [22]. Comprehensive tunable diode laser absorption spectroscopy (TDLAS)-driven monitoring techniques spanning the methane absorption lines of 1635-1675 nm [19] could prevent fatal explosions (i.e. San Bruno, California [22]), limit the environmental impact of natural gas, as well as benefit the bottom line of the energy sector. However, such systems are bulky and expensive which limits its implementation. Tombez et al. circumvented the above with a silicon photonic waveguide sensor; the laser source of the integrated system is however located off-chip [23]. The addition of a chip-based tunable laser source that cover the molecular fingerprints of methane can increase the extent of integration in the system. The above are some of the more prominent applications of the wavelength region. Instances of other applications, while not exhaustive, include eye surgery [24], deep-tissue imaging [25–26], gas sensing (i.e. C_2H_2, C_2H_4, C_3H_8) [27–29], free-space communication and LIDAR [30]. Thereby, development into the wavelength region presents huge opportunities.

Advanced silicon manufacturing [31–32], and high-index contrast between silicon waveguides and its oxide has permitted low-loss, compact microring resonators (MRRs) to be fabricated [33–34]. The effective optical path length in MRRs at resonance can be extended beyond its physical length. When cascaded together, highly-selective Vernier filters with narrow full half-width maximum (FWHM), high Q-factors and large modal transmittance difference (MTD) can be realized [35].

In this work, we report for the first time, a III-V/silicon hybrid ring external cavity (SHREC) wavelength-tunable laser diode operating from 1647-1690 nm; two MRRs and a closed-loop MMI makes up the SHREC. Fine-tuning resolution of 0.5 nm is demonstrated. The maximum output power is 31.1 mW, corresponding to a maximum side-mode suppression ratio (SMSR) of 46.01 dB. By integrating a 35 km-long recirculating fiber-loop into the delayed self-heterodyne interferometer (DSHI) measurement technique [36], the laser linewidth is estimated to be 0.7 kHz. The characteristics of this laser is indicated in Fig. 1, in comparison to previous work. This

demonstration extends the reach of III-V/silicon hybrid/heterogeneous lasers with sub-kHz laser linewidth beyond the L-band, into the 1650 nm wavelength region.

Furthermore, the laser output power is favorable as shown by the inset of Fig. 1. This work is organized as follows. Firstly, device design is elaborated. Following, the Vernier filter is characterized theoretically and experimentally. The optical emission of the SOA is measured. Laser performance in terms of light-current-voltage (L-I-V), SMSR, discrete/fine wavelength tuning and linewidth is provided.

2. Device design

The 3-D schematic of the III-V/SHREC wavelength-tunable laser diode is illustrated in Fig. 2(a). Figures 2(b)-(e) shows the 3-D schematic of the III-V/SHREC, MRR-bus waveguide coupling regions and micrograph images of the semiconductor optical amplifier (SOA), SHREC respectively.
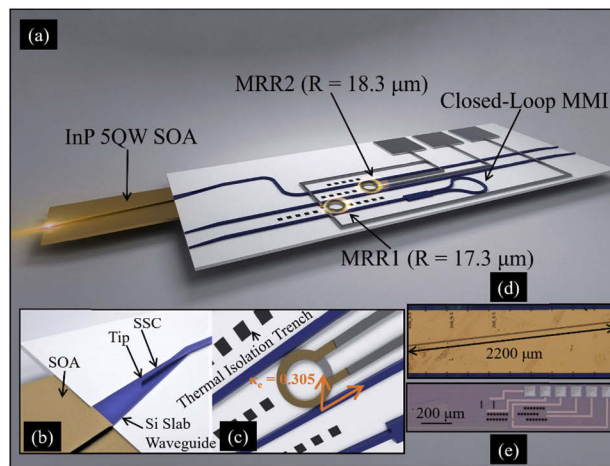
Fig. 2. (a) 3-D schematic of the III-V/SHREC wavelength-tunable laser diode. (b) 3-D schematic of the III-V/SHREC coupling region via the silicon slab waveguide and SSC. (c) 3-D schematic of the MRR-bus waveguide coupling region in the SHREC. (d) Micrograph image of the SOA. (e) Micrograph image of the SHREC.

Hybrid integration between the SOA and the SHREC is realized via the silicon slab waveguide and spot-size converter (SSC) to form the laser cavity; the silicon slab waveguide enables mode matching at the facet of the SOA, and the SSC with a tip width of 100 nm converts the silicon slab to strip waveguide mode (Fig. 2(b)). The length of the silicon slab waveguide and SSC are 20 and 200 μm respectively. Cross-sectional dimensions of the silicon strip and slab waveguide are 0.5×0.22 and 6×0.07 μm^2 respectively [37]. With regards to the SHREC, thermo-optic phase shifters are mounted on the two MRRs with radii of 17.3 (mrr1) and 18.3 (mrr2) μm enabling wavelength-selective filtering through the overlap of the MRR resonances, giving rise to a Vernier peak (Fig. 3(a)). The closed-loop MMI, optimized at $\lambda = 1670$ nm, facilitates reflectance of the filtered Vernier spectra; MMI width, length, gap between output tapers, taper width and length are 6, 29.2, 3.14, 1.5 and 50 μm respectively. The SOA addresses optical emission and amplification, the SHREC facilitates wavelength-selective feedback. The laser longitudinal mode that most closely matches the wavelength (λ_V) of the Vernier peak (Fig. 3(a)) will experience the least cavity loss, and thereby, lase via mode competition. Laser cavity extension is facilitated primarily through the Vernier effect [3]. Lasing output is indicated at the facet of the SOA in Fig. 2(a).
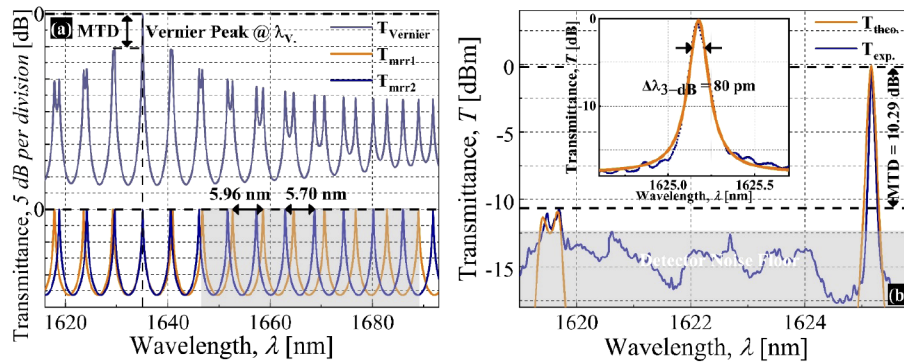
Fig. 3. (a) Computed transmittances of mrr1, 2 and Vernier filter when $H_{mrr1} = H_{mrr2} = 0$ mW. (b) Measured and corresponding computed Vernier transmittances when $H_{mrr1} = 7.792$ mW, $H_{mrr2} = 0$ mW; inset shows the measured Vernier peak, indicating the FWHM.

3. Experimental characterization of constituent components (III-V and silicon)

3.1. Wavelength selectivity via the Vernier effect

The silicon photonic chip is fabricated via a CMOS process line utilizing the immersion lithography system. Following the fabrication of the strip and slab waveguide, 1.2 µm-thick SiO_2 cladding is deposited to isolate the waveguide mode from the metal, preventing waveguide loss via metal absorption (0.12 and 2 µm-thick TiN heating and Al routing layers respectively). The computed transmittances of mrr1 and 2 with free-spectral ranges (FSRs) of 5.96 and 5.70 nm respectively, no heater power applied on mrr1 and mrr2 ($H_{mrr1} = H_{mrr2} = 0$ mW) are shown in the lower-half of Fig. 3(a); the tuning range of the reported laser is shaded. Via the product of the two MRRs transmittances, the Vernier spectra is illustrated at the upper-half of Fig. 3(a). The FWHM of the Vernier peak as well as the modal transmittance difference (MTD), the contrast in transmittance between the Vernier peak and its adjacent peaks, determine the extent of wavelength-selectivity with regards to the passive cavity. The transmittance at the Vernier peak refers to the single-trip insertion loss of the Vernier filter. The MTD and insertion loss are inversely related to the coupling strength (κ_e) between the bus waveguide and the MRR (Fig. 2(c)); the higher the κ_e, the lower the MTD and insertion loss, and vice versa. In addition, lowering waveguide propagation loss will narrow the FWHM and reduce the insertion loss of the Vernier peak.

As the range (1500-1630 nm) of our benchtop tunable light source does not fall within the demonstrated operating range of this work (1647-1690 nm), the Vernier spectra is characterized at its closest source-supported Vernier peak (Fig. 3(b)). The designed κ_e is 0.305. When $H_{mrr1} = 7.792$ mW and $H_{mrr2} = 0$ mW, a Vernier peak can be obtained at $\lambda = 1625.17$ nm, with an MTD of 10.29 dB and insertion loss of 0.48 dB. The propagation loss of the silicon strip waveguides that constitute the MRRs is estimated to be 0.52 dB/cm. By factoring the above parameters into the Vernier spectra computation ($T_{theo.}$), good agreement is obtained with regards to experimental data ($T_{exp.}$); the noise floor of the photodetector is indicated by the shaded region. The measured FWHM of the Vernier peak is shown at the inset of Fig. 3(b) to be 80 pm. This is sufficient for the filtering of a single laser cavity longitudinal mode at the Vernier peak as confirmed by the data from the laser linewidth measurement (Fig. 9(b)). The MMI has a simulated insertion loss of 0.12 dB at $\lambda = 1670$ nm where it is optimized, and a maximum simulated insertion loss of 0.18 dB over the operating range of the laser in this work.

3.2. SOA optical emission

The SOA is based on five InAlGaAs quantum wells, designed to operate with a peak near 1670 nm; its fabrication process flow is elaborated in our previous work [38]. The waveguide (5.0 [width] × 1.0 [height] μm^2) is angled at 6.5°, and single layer of Al_2O_3 anti-reflection coatings are deposited on both facets of the SOA (reflection < 1.5%) to maintain the single-mode stability of the laser [39], increase laser output power and preventing the SOA from self-lasing [40]. The length of the III-V waveguide is 2.2 mm (Fig. 2(d)). For spectra characterization throughout this work, the light emission from the facet of the SOA is coupled to the optical spectra analyzer (OSA) via a lensed fiber. Figure 4 illustrates the spontaneous emission (SE) spectra of the SOA under bias currents (I_{bias}) of 200, 300, 400 and 440 mA; thermal saturation occurs when I_{bias} > 400 mA. Extensive suppression in F-P oscillations is achieved as evident of a gain ripple (GR) lower than 0.26 dB (Fig. 4, inset).
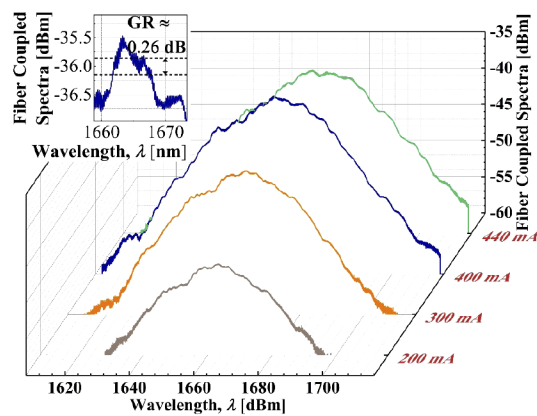

Fig. 4. SOA SE when I_{bias} = 200, 300, 400, 440 mA; inset shows GR of SE.

## 4. Experimental characterization of laser diode

4.1. Light-current-voltage, side-mode suppression ratio

The laser is characterized by placing the silicon photonic and SOA chip on two separate precision alignment stages, each connected to a thermoelectric controller. The slant angle of the silicon slab waveguide is 11° via Snell's law, in consideration of the slant angle of the III-V waveguide (6.5°). The coupling loss between the hybrid integration of the SOA and the SHREC (Fig. 2(b)) is measured to be 2.4 dB; this represents the loss from the SOA to the silicon slab waveguide, then the SSC. The L-I-V curve of the laser is indicated in Fig. 5. Light emission is coupled directly into the opening of the photodetector which integrates the sum of the power under the lasing spectra for laser power characterization; the setup enables all light emission to be coupled into the photodetector, thereby, the coupling loss of laser power off-chip, to the photodetector is negligible. Room temperature (293 K)-continuous wave (RT-CW) operation was achieved with a threshold current (I_{th}) of 296 mA, and a maximum demonstrated laser output power of 31.03 mW when I_{bias} = 400 mA, beyond which, thermal saturation occurs, leading to a decrease in laser power. The slope efficiency (η_s) is 0.312 W/A and the wall-plug efficiency (WPE) of the laser is 5.6% when I_{bias} = 400 mA. Figure 6 shows the evolution of the lasing spectra as a function of I_{bias} = 300-440 mA in step-sizes of 20 mA; values of SMSR are plotted at the inset. Mentioned above, spectra characterization in this work is performed by coupling the laser output to a lensed fiber, which is then connected to an OSA; the coupling loss between the laser output facet and lensed fiber is 10 dB in our setup. As seen from the inset of Fig. 6 (I_{bias} = 300-440

mA), the maximum value of SMSR is 46.01 dB when I_{bias} = 400 mA, beyond which, degradation sets in due to thermal saturation and a subsequent drop in laser power. This is shown by the L-I curve presented in Fig. 5.
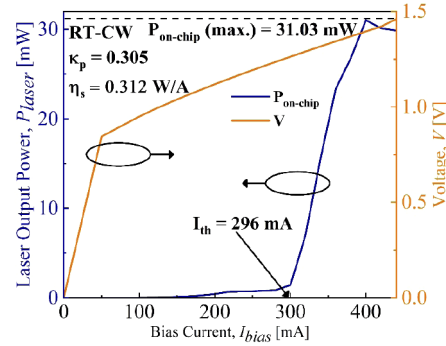

Fig. 5. L-I-V of the laser diode from I_{bias} = 0-440 mA.
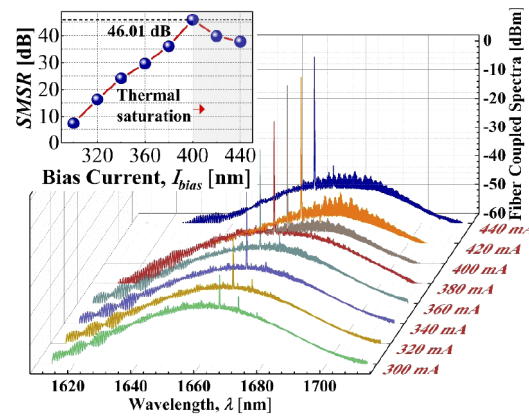
Fig. 6. Evolution of lasing spectra from I_{bias} = 300–440 mA (step-size = 20 mA); inset shows the SMSR against I_{bias}.

4.2. *Discrete/fine laser wavelength tuning*

Laser tuning operation can be understood from the shaded lower-half of Fig. 3(a), via the positions of the two MRR resonances, with respect to one another. The discrete tuning range of the laser is 1647-1690 nm with a SMSR of higher than 34.41 dB (Fig. 7(a)); the value of H_{mrr2} for each discrete laser wavelength tuning step is shown in Fig. 7(b). With regards to discrete tuning of laser wavelength, one of the two heaters are used. For instance, in this work, by increasing H_{mrr2}, the resonance of mrr2 will shift towards longer wavelengths and overlap with that of mrr1, redshifting the Vernier peak. Thereby, the lasing will occur at λ_V. via mode competition with an FSR that correspond to mrr1. The opposite will be true if H_{mrr1} is considered; Vernier peak and subsequently lasing wavelength will blueshift in step sizes according to the FSR of mrr2 when H_{mrr1} is increased. However, due to the relative positioning of the two MRR resonances in Fig. 3(a), discrete tuning of laser wavelength via H_{mrr1} will require more heater power in comparison to H_{mrr2} as the resonance of mrr1 will be required to redshift up to approximately one FSR of mrr2.
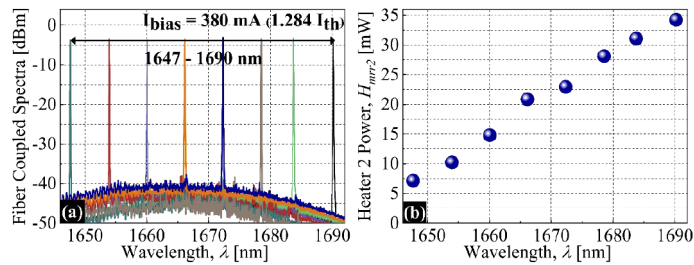
Fig. 7. (a) Superimposed, discrete lasing spectra of 1647-1690 nm when I_{bias} = 380 mA. (b) H_{mrr2} corresponding to each discrete tuning wavelength.

Fine tuning of laser wavelength can be achieved through the thermo-optic control of the two heaters ($H_{mrr1\&2}$). In this work, continuous fine tuning with resolution of 0.5 nm is demonstrated in Fig. 8(a) from 1666.1-1668.6 nm; the thermo-optic tuning efficiency of mrr1/mrr2 resonance is 11.718 mW/nm. Such precision is required in applications such as dense wavelength division multiplexing (DWDM) and spectroscopy. The values of $H_{mrr1\&2}$ corresponding to each fine laser wavelength tuning step in the wavelength region of 1666.1-1668.6 nm is plotted in Fig. 8(b).
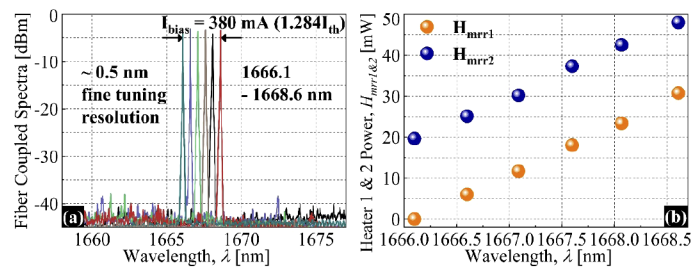

Fig. 8. (a) Superimposed, fine lasing spectra (resolution = 0.5 nm) of 1666.1-1668.6 nm when I_{bias} = 380 mA. (b) $H_{mrr1\&2}$ corresponding to each fine tuning wavelength.

4.3. Laser linewidth

With regards to prior linewidth measurement amongst hybrid/heterogeneous III-V/silicon lasers, the delayed self-heterodyne interferometer (DSHI) technique is used due to the lack of resolution of the OSA. Typical values of implemented optical delay path is 25 km of silica fiber, which supports the characterization of laser linewidth down to several kHz. In this work, enabled by the low propagation loss of the 1650 nm wavelength region in silica fibers, the DSHI technique is modified by integrating a 35 km-long recirculating fiber loop, as illustrated in Fig. 9(a), facilitating extensive optical delay path. The I_{bias}, emission wavelength and corresponding output power are 380 mA, 1666.01 nm and 26.79 mW respectively during laser linewidth characterization; the laser is driven by a low noise current source. The laser emission is coupled into an isolator via a lensed fiber, then, a 1×2 coupler (10:90), where 10% of the light power is directed to the OSA to monitor the single-mode and wavelength stability of the laser. The remaining light power (90%) is connected to the input port of a 2×2 coupler (50:50). One of the output ports of the 2×2 coupler is connected to a high-speed photodiode (PD), then RF amplifier and after which, the electrical spectrum analyzer (ESA). The recirculating fiber loop is formed by linking the other output to input port of the 2×2 coupler in the order: first the fiber polarization controller (FPC), followed by a 35 km-long fiber loop, then an acoustic optic modulator (AOM). As the AOM operates at 80 MHz, beat signals would be present at frequencies of 80n MHz, where n refers to

the number of round trips that light makes through the fiber loop and 80 MHz is the frequency shift by the AOM. During data acquisition, the ESA is averaged five times.
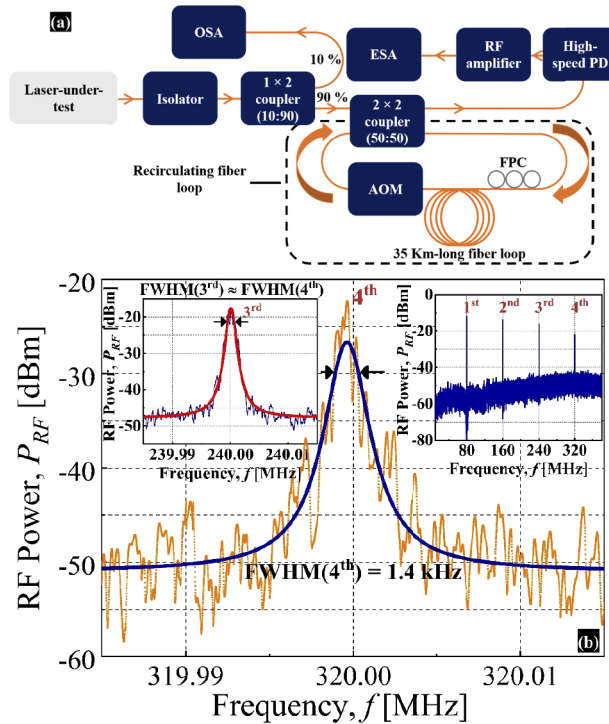
Fig. 9. (a) Schematic setup of recirculating fiber loop (35 km) integrated DSHI measurement technique. (b) Laser linewidth measured using the recirculating fiber loop integrated DSHI measurement technique. The FWHM of the beat signal is 1.4 kHz at f = 320 MHz, corresponding to ΔL = 140 km. Insets show the beat signal at f = 240 MHz (ΔL = 105 km) and clear and distinct beat signals at f = 80, 160, 240, 320 MHz.

As presented in Fig. 9(b), the FWHM of the beat signal is 1.4 kHz at f = 320 MHz, corresponding to an estimated laser linewidth of 0.7 kHz assuming a Lorentzian line shape; the fiber delay length (ΔL) at f = 320 MHz is 140 km. As shown in the inset of Fig. 9(b), clear and distinct beat signals at f = 80, 160, 240, 320 MHz when ΔL = 35, 70, 105, 140 km respectively is observed as expected. The estimated laser linewidth at f = 240 MHz agrees closely to that obtained at f = 320 MHz (Fig. 9(b), inset). This is because ΔL = 105, 140 km are longer than the coherence length of the laser. Indications of coherent beating are observed at f = 80, 160 MHz [41], as the ΔL = 35, 70 km are shorter than the coherence length of the laser.

5. Conclusion

The application-rich window about 1650 nm has been overlooked with the focus near the O and C-bands, as well as more recently, the 2 μm waveband [37,42–44]. In this work, we report a high performance III-V/SHREC wavelength-tunable laser diode operating from 1647-1690 nm for the first time. RT-CW operation is achieved with a maximum demonstrated output power of 31.1 mW, corresponding to a SMSR of 46.01 dB. The laser emission is highly-coherent, with an estimated linewidth of 0.7 kHz. This work extends the coverage of III-V/silicon hybrid/heterogeneous lasers with sub-kHz linewidth beyond the L-band, into the 1650 nm wavelength region. Further

improvement in laser linewidth can be achieved through the negative optical feedback mechanism [2,3].

Disclosures

The authors declare that there are no conflicts of interest.

References

1. T. Komljenovic, M. Davenport, J. Hulme, A. Y. Liu, C. T. Santis, A. Spott, S. Srinivasan, E. J. Stanton, C. Zhang, and J. E. Bowers, "Heterogeneous Silicon Photonic Integrated Circuit," J. Lightwave Technol. **34**(1), 20–35 (2016).
2. M. A. Tran, D. Huang, and J. E. Bowers, "Tutorial on narrow linewidth tunable semiconductor lasers using Si/heterogeneous integration," APL Photonics **4**(11), 111101 (2019).
3. K. Boller, A. van Rees, Y. Fan, J. Mak, R. E. M. Lammerink, C. A. A. Franken, P. J. M. van der Slot, D. A. I. Marpaung, C. Fallnich, J. P. Epping, R. M. Oldenbeuving, D. Geskus, R. Dekker, I. Visscher, R. Grootjans, C. G. H. Roeloffzen, M. Hoekman, E. J. Klein, A. Leinse, and R. G. Heideman, "Hybrid Integrated Semiconductor Lasers with Silicon Nitride Feedback Circuits," Photonics **7**(1), 4 (2019).
4. Y. Fan, A. van Rees, P. J. M. van der Slot, J. Mak, R. M. Oldenbeuving, M. Hoekman, D. Geskus, C. G. H. Roeloffzen, and K. Boller, "Hybrid integrated InP-Si₃N₄ diode laser with a 40-Hz intrinsic linewidth," Opt. Express **28**(15), 21713–21728 (2020).
5. D. Huang, M. A. Tran, J. Guo, J. Peters, T. Komljenovic, A. Malik, P. A. Morton, and J. E. Bowers, "High-power sub-kHz linewidth lasers fully integrated on silicon," Optica **6**(6), 745–752 (2019).
6. S. Yang, Y. Zhang, D. W. Grund, G. A. Ejzak, Y. Liu, A. Novack, D. Prather, A. E. Lim, G. Lo, T. Baehr-Jones, and H. Hochberg, "A single adiabatic microring-based laser in 220 nm silicon-on-insulator," Opt. Express **22**(1), 1172–1180 (2014).
7. C. T. Santis, S. T. Steger, Y. Vilenchik, A. Vasilyev, and A. Yariv, "High-coherence semiconductor lasers based on integral high Q-resonators in hybrid Si/platforms," Proc. Natl. Acad. Sci. U. S. A. **111**(8), 2879–2884 (2014).
8. P. Dong, T. Hu, T. Liow, Y. Chen, C. Xie, X. Luo, G. Lo, R. Kopf, and A. Tate, "Novel integration technique for silicon/hybrid laser," Opt. Express **22**(22), 26854–26861 (2014).
9. N. Kobayashi, K. Sato, M. Namiwaka, K. Yamamoto, S. Watanabe, T. Kita, H. Yamada, and H. Yamazaki, "Silicon Photonic Hybrid Ring-Filter External Cavity Wavelength Tunable Lasers," J. Lightwave Technol. **33**(6), 1241–1246 (2015).
10. T. Kita, R. Tang, and H. Yamada, "Narrow Spectral Linewidth Silicon Photonic Wavelength Tunable Laser Diode for Digital Coherent Communication System," IEEE J. Sel. Top. Quantum Electron. **22**(6), 23–34 (2016).
11. J. Zhang, Y. Li, S. Dhoore, G. Morthier, and G. Roelkens, "Unidirectional, widely-tunable and narrow-linewidth heterogeneously integrated-on-silicon laser," Opt. Express **25**(6), 7092–7100 (2017).
12. B. Stern, X. Ji, A. Dutt, and M. Lipson, "Compact narrow-linewidth integrated laser based on a low-loss silicon nitride ring resonator," Opt. Lett. **42**(21), 4541–4544 (2017).
13. H. Guan, A. Novack, T. Galfsky, Y. Ma, S. Fathololoumi, A. Horth, T. M. Huynh, J. Roman, R. Shi, M. Caverley, Y. Liu, T. Baehr-Jones, J. Bergman, and M. Hochberg, "Widely-tunable, narrow-linewidth /silicon hybrid external-cavity laser for coherent communication," Opt. Express **26**(7), 7920–7933 (2018).
14. C. Xiang, W. Jin, J. Guo, J. D. Peters, M. J. Kennedy, J. Selvidge, P. A. Morton, and J. E. Bowers, "Narrow-linewidth /Si/Si₃N₄ laser using multilayer heterogeneous integration," Optica **7**(1), 20–21 (2020).
15. Y. Zhu, S. Zeng, and L. Zhu, "Optical beam steering by using tunable, narrow-linewidth butt-coupled hybrid lasers in a silicon nitride photonics platform," Photonics Res. **8**(3), 375–380 (2020).
16. J. X. B. Sia, W. Wang, X. Guo, J. Zhou, Z. Zhang, M. S. Rouifed, X. Li, Z. L. Qiao, C. Y. Liu, C. Littlejohns, G. T. Reed, and H. Wang, "Mid-Infrared, Ultra-Broadband, Low-Loss, Compact Arbitrary Power Splitter Based on Adiabatic Mode Evolution," IEEE Photonics J. **11**(2), 1–11 (2019).
17. B. Jeżewski, A. Broda, I. Sankowska, A. Kuźmicz, K. Gołaszewska-Malec, K. Czuba, and J. Muszalski, "Membrane external-cavity surface-emitting laser emitting at 1640 nm," Opt. Lett. **45**(2), 539–542 (2020).
18. G. Crosnier, D. Sanchez, S. Bouchoule, P. Monnier, G. Beaudoin, I. Sagnes, R. Raj, and F. Raineri, "Hybrid indium phosphide-on-silicon nanolaser diode," Nat. Photonics **11**(5), 297–300 (2017).
19. S. Chen, Y. Jung, S. Alam, D. J. Richardson, R. Sidharthan, D. Ho, S. Yoo, and J. M. O. Daniel, "Ultra-short wavelength operation of thulium-doped fiber amplifiers and lasers," Opt. Express **27**(25), 36699–36707 (2019).
20. Z. Li, Y. Jung, J. M. O. Daniel, N. Simakov, M. Tokurakawa, P. C. Shardlow, D. Jain, J. K. Sahu, A. M. Heidt, W. A. Clarkson, S. U. Alam, and D. J. Richardson, "Exploiting the short wavelength gain of silica-based thulium-doped fiber amplifiers," Opt. Lett. **41**(10), 2197–2200 (2016).
21. S. V. Firstov, S. V. Alyshev, K. E. Riumkin, V. F. Khopin, A. N. Guryanov, M. A. Melkumov, and E. M. Dianov, "A 23-dB bismuth-doped optical fiber amplifier for a 1700-nm band," Sci. Rep. **6**(1), 28939 (2016).

22. P. Patel, "Monitoring methane," ACS Cent. Sci. **3**(7), 679–682 (2017).
23. L. Tombez, E. J. Zhang, J. S. Orcutt, S. Kamlapurkar, and W. M. J. Green, "Methane absorption spectroscopy on a silicon photonic chip," Optica **4**(11), 1322–1325 (2017).
24. C. Crotti, F. Deloison, F. Alahyane, F. Aptel, L. Kowalczuk, J. M. Legeais, D. A. Peyrot, M. Savoldelli, and K. Plaman, "Wavelength optimization in femtosecond laser corneal surgery," Invest. Ophthalmol. Visual Sci. **54**(5), 3340–3349 (2013).
25. N. G. Horton, K. Wang, D. Kobat, C. G. Clark, F. W. Wise, C. B. Schaffer, and C. Xu, "In vivo three-photon microscopy of subcortical structures within an intact mouse brain," Nat. Photonics **7**(3), 205–209 (2013).
26. P. Cadroas, L. Abdeladim, L. Kotov, M. Likhachev, D. Lipatov, D. Gaponov, A. Hideur, M. Tang, J. Livet, W. Supatto, E. Beaurepaire, and S. Février, "All-fiber femtosecond laser providing 9 nJ, 50 MHz pulses at 1650 nm for three-photon microscopy," J. Opt. **19**(6), 065506 (2017).
27. K. Zheng, C. Zheng, N. Ma, Z. Liu, Y. Yang, Y. Zhang, Y. Wang, and F. K. Tittel, "Near-Infrared Broadband Cavity-Enhanced Spectroscopic Multigas Sensor Using a 1650 nm Light Emitting Diode," ACS Sens. **4**(7), 1899–1908 (2019).
28. X. Cui, F. Dong, Z. Zhang, H. Xia, T. Pang, P. Sun, B. Wu, S. Liu, L. Han, Z. Li, and R. Yu, *Green Electronics: Environmental Application of High Sensitive Gas Sensors with Tunable Diode Absorption Spectroscopy* (Intech Open, 2017).
29. J. Yoo, N. Traina, M. Halloran, and T. Lee, "Minute Concentration Measurements of Simple Hydrocarbon Species Using Supercontinuum Laser Absorption Spectroscopy," Appl. Spectrosc. **70**(6), 1063–1071 (2016).
30. K. Wang, C. Gao, Z. Lin, Q. Wang, M. Gao, S. Huang, and C. Chen, "1645 nm coherent Doppler wind lidar with a single-frequency Er-YAG laser," Opt. Express **28**(10), 14694–14704 (2020).
31. J. Sun, R. Kumar, M. Sakib, J. B. Driscoll, H. Jayatilleka, and H. Rong, "A 128 Gb/s PAM4 Silicon Microring Modulator With Integrated Thermo-Optic Resonance Tuning," J. Lightwave Technol. **37**(1), 110–115 (2019).
32. W. Jin, D. D. John, J. F. Bauters, T. Bosch, B. J. Thibeault, and J. E. Bowers, "Deuterated silicon dioxide for heterogeneous integration of ultra-low-loss waveguides," Opt. Lett. **45**(12), 3340–3343 (2020).
33. A. Griffith, J. Cardenas, C. B. Poitras, and M. Lipson, "High quality factor and high confinement silicon resonators using etchless process," Opt. Express **20**(19), 21341–21345 (2012).
34. W. Bogaerts, P. De Heyn, T. Van Vaerenbergh, K. De Vos, S. K. Selvaraja, T. Claes, P. Dumon, P. Bienstman, D. Van Thourhout, and R. Baets, "Silicon microring resonators," Laser Photonics Rev. **6**(1), 47–73 (2012).
35. J. C. C. Mak, T. Xue, Z. Yong, and J. K. S. Poon, "Wavelength Tunable Matched-Pair Vernier Multi-Ring Filters Using Derivative-Free Optimization Algorithms," IEEE J. Sel. Top. Quantum Electron. **26**(5), 1–12 (2020).
36. H. Tsuchida, "Simple technique for improving the resolution of the delayed self-heterodyne method," Opt. Lett. **15**(11), 640–642 (1990).
37. J. X. B. Sia, W. Wang, Z. Qiao, X. Li, X. Guo, J. Zhou, C. G. Littlejohns, Z. Zhang, C. Liu, G. T. Reed, and H. Wang, "Compact silicon photonic hybrid ring external cavity (SHREC)/InGaSb-AlGaAsSb wavelength-tunable laser diode operating from 1881-1947nm," Opt. Express **28**(4), 5134–5146 (2020).
38. X. Li, H. Wang, Z. Qiao, X. Guo, W. Wang, J. X. B. Sia, G. I. Ng, Y. Zhang, Z. Niu, C. Tong, and C. Liu, "High temperature characteristics of a 2 μm InGaSb/AlGaAsSb passively mode-locked quantum well laser," Appl. Phys. Lett. **114**(22), 221104 (2019).
39. N. Fujioka, T. Chu, and M. Ishizaka, "Compact and Low Power Consumption Hybrid Integrated Wavelength Tunable Laser Module Using Silicon Waveguide Resonators," J. Lightwave Technol. **28**(21), 3115–3120 (2010).
40. J. Amirloo, S. S. Saini, and M. Dagenais, "Comprehensive study of antireflection coatings for mid-infrared lasers," J. Vac. Sci. Technol., A **34**(6), 061505 (2016).
41. "Laser Spectral Linewidth," https://www.sevensix.co.jp/wordpress/wp-content/uploads/2017/07/Linewidth-Application-Note-Version-1-1-October-2013.pdf.
42. J. Guo, J. Li, C. Liu, Y. Yin, W. Wang, Z. Ni, Z. Fu, H. Yu, Y. Xu, Y. Shi, Y. Ma, S. Gao, L. Tong, and D. Dai, "High-performance silicon-graphene hybrid plasmonic waveguide photodetectors beyond 1.55 μm," Light: Sci. Appl. **9**(1), 29 (2020).
43. D. E. Hagan, M. Ye, P. Wang, J. C. Cartledge, and A. P. Knights, "High-speed performance of a TDFA-band micro-ring resonator modulator and detector," Opt. Express **28**(11), 16845–16856 (2020).
44. J. X. B. Sia, W. Wang, X. Guo, J. Zhou, Z. Zhang, X. Li, Z. L. Qiao, C. Y. Liu, C. Littlejohns, G. T. Reed, and H. Wang, "SiN-SOI Multilayer Platform for Prospective Applications at 2 μm," IEEE Photonics J. **11**(6), 6603809 (2019).